

Learning 3D Affordances for Blade Insertion in Cluttered Stowing

Tianyu Li, Harpreet Sawhney, Minju Jung, Aditya Mehrotra, Kunal Mehrotra,
and Mudit Agrawal

Amazon Robotics, USA

Corresponding author: hasawhne@amazon.com

Abstract. Many manipulation tasks require reasoning about **free-space affordances**: discovering volumes where an extended rigid tool can safely navigate, complementary to surface contact affordances for grasping. Robotic stowing is a canonical instance, where a blade must sweep items aside inside cluttered fabric bins to create insertion space. Production stow systems generate millions of such episodes, but standard approaches with unimodal data infer affordances as $SE(3)$ pose distributions, a geometric question asked in the wrong domain. **VulcanVoxel** keeps inference spatial: a masked autoencoder over 3D occupancy fields reconstructs blade occupancy conditioned on scene geometry, computing feasibility locally at each voxel and recovering multi-modal predictions from unimodal data. Blade affordances are spatial objects, subsets of 3D space defined by geometric feasibility. Pose parameters carry no structure for reasoning whether unobserved placements are feasible, and standard generative objectives including flow matching faithfully learn the unimodal distribution produced by execution policies and cannot recover geometric alternatives. Trained on 10,000 real warehouse stow episodes without human annotation, VulcanVoxel achieves top-5 coverage of 0.89 versus 0.71 for the best pose-based baseline, with a distilled student providing RGB→voxel inference in 30 ms vs. 1.4 s for voxel→voxel. We have released a dataset of real blade insertion cycles with RGB-D observations and pose trajectories at https://www.armbench.com/blade_insertion.html.

Keywords: Affordances · 3D Learning · Robot Learning

1 Introduction

Robotic stowing into densely cluttered flexible fabric bins [9] requires navigating a rigid tool through narrow gaps to create space by sweeping in-bin items. This is a **free-space affordance** problem: discovering volumes of 3D space a tool can occupy given surrounding geometry. It is complementary to the well-studied surface contact affordance problem of where to touch an object to grasp or articulate it. Surface affordances ground predictions on object geometry with strong local cues. Free-space affordances must reason about navigable volumes constrained by surrounding surfaces and bin walls, with no surface to anchor



Fig. 1: Blade insertion for stowing. Top: Initial bin state, blade approach, and insertion into a densely cluttered bin. **Bottom:** Blade navigating tight gaps while sweeping. Precise 3D geometric reasoning avoids damaging items/bin walls while reaching sufficiently deep to start sweeping items to create space.

predictions to. Blade insertion for robotic stowing is a canonical instance, studied here with real manipulation data.

Stow executes millions of stows annually with 67% blade insertion success [9]. As shown in Fig.,1, creating space requires inserting the blade into an occupied bin to sweep existing items aside without damaging items or deforming bin walls. A single RGB-D camera provides a fixed viewpoint with limited coverage of occluded regions demanding that blade insertion inferences be robust to partial observability and depth noise. A curated subset of production episodes with paired RGB-D observations and executed SE(3) poses presents a scalable opportunity for data-driven affordance learning. Exploiting this data is non-trivial: each stow executes a single insertion strategy per bin state, despite most states affording multiple geometrically valid solutions (Sec.,4.3).

The bottleneck is not model capacity or data scale but the domain in which affordance inference is performed. Blade affordances are spatial objects, subsets of 3D Euclidean space defined by geometric feasibility. The goal is to find volumes in a bin for blade occupancy as an approximation of optimal blade insertions. SE(3) poses index individual tool placements, not spatial affordance structure. Inferring affordances as pose distributions displaces reasoning from the domain where geometric feasibility is defined: whether a blade fits is a question about what it occupies in 3D space, not about pose parameters. Flow matching over SE(3) poses collapses to unimodal predictions because the pose data is unimodal.

The resolution is to keep inference in the spatial domain. Representing blade affordances as 3D occupancy fields and training a masked autoencoder to reconstruct blade occupancy conditioned on scene geometry forces reasoning where geometric feasibility is natively defined. Executed stows sample only a subset of geometrically valid placements. By reasoning explicitly about occupancy, the model discovers alternative free-space configurations rather than reproducing observed behaviors, activating occupancy wherever local geometry accommodates the blade independently across locations. This generates implicit supervision for

never executed geometrically consistent configurations, recovering multimodal predictions from unimodal data. This principle extends to failed stow episodes: the model can still identify free-space volumes from scene geometry alone, turning failures into training signal rather than discarded data.

VulcanVoxel implements this as a masked autoencoder over multi-channel 3D occupancy fields trained on 10K real blade insertion episodes without human annotation. Predicted blade occupancy is converted to SE(3) poses via geometric scoring, deferring pose extraction as a post-hoc projection after spatial reasoning. A distilled RGB student achieves 30,ms inference, confirming affordances are grounded in visually accessible geometric features rather than execution-specific patterns. VulcanVoxel achieves top-5 pose coverage of 0.89 versus 0.71 for the best pose-based baseline—at least one of five predicted poses is geometrically valid in 89% of scenes—and matches production on single-prediction accuracy. Our contributions are:

1. **Spatial inference for free-space affordance learning.** Blade affordances as spatial objects inferred in 3D space rather than as SE(3) poses.
2. **Representational analysis.** Systematic comparison across input and output representations, and training objectives establishes which properties are necessary for multi-modal prediction from unimodal data, with Cov_5 as a quantitative metric for the operational value of diversity (Sec.4.3).
3. **Generalization to failed episodes.** VulcanVoxel reasons about geometric feasibility directly in voxel space, and identifies free-space voxels even when the production system found no viable strategy, turning failed episodes into informative training signals.
4. **StowAffordance dataset.** To our knowledge the first large-scale dataset of real manipulation cycles with RGB-D and executed tool insertion trajectories, released at https://www.armbench.com/blade_insertion.html.

2 Related Work

Affordance Learning for Manipulation. Prior affordance learning methods ground spatial priors on object geometry or 2D spatial maps. Where2Act [15] and VAT-Mart [23] predict per-point action likelihoods for articulated objects; GIFT [19] and VRB [1] learn interaction keypoints from contact data and ego-centric video; Transporter Networks [24] predict pick-and-place as 2D attention maps; SAGA [5] grounds affordances as 3D heatmaps for mobile manipulation; UAD [18] and environment-aware methods [22] extend affordance learning to foundation model distillation and occlusion respectively. All ground predictions on object surfaces. Blade insertion requires the complementary problem: volumetric free-space affordances that reason about where a rigid tool can navigate optimally, motivating different representations, objectives, and evaluation criteria.

3D Scene Representations for Robot Learning. 3D Diffuser Actor [10] and Adapt3R [21] condition policies on point clouds and lifted 2D features respectively; Neural Descriptor Fields [17] encode SE(3)-equivariant representations for

few-shot manipulation; D3Fields [20] fuses multi-view features into dynamic descriptor fields for zero-shot rearrangement; 3D flow matching [7] extends generative modeling to 3D action spaces. These methods recover diverse strategies when training data is genuinely multi-modal, but collapse to unimodal predictions on production data because the limitation lies in the $SE(3)$ pose representation, not the generative architecture. CabiNet [6] is the closest architectural relative, learning voxel representations for collision checking in cluttered rearrangement, but addresses *general-purpose feasibility checking* rather than *task-specific affordance learning*. Collision-free space is necessary but not sufficient for blade insertion; our model learns which geometrically valid configurations are operationally preferable given constraints encoded in production demonstrations. Our distillation shares the spirit of 2D-to-3D feature lifting [20, 21] but distills from a voxel teacher rather than lifting multi-view features directly.

Occupancy Prediction and Masked Autoencoders. Occupancy networks [13] establish the paradigm of learning implicit 3D representations as continuous functions; scene occupancy methods [2] extend this to semantic 3D completion from single views. Both predict *scene* occupancy from visual input. VulcanVoxel addresses a different problem: predicting *tool* occupancy conditioned on observed scene occupancy. Masked Autoencoders [8, 16] demonstrate that masked reconstruction is a powerful self-supervised objective for visual representations. VulcanVoxel extends this to 3D occupancy fields with channel masking over semantic entities (wall, object, blade) rather than spatial patch masking, directly matching the conditional structure of the affordance query.

3 Approach

Blade insertion affords multiple geometrically valid configurations per bin state, yet production data records a single executed strategy per stow. $SE(3)$ poses record where the blade was sent, not the spatial affordance structure that makes those placements valid. **VulcanVoxel** resolves this by inferring affordances in their native domain: a masked autoencoder over multi-channel 3D occupancy fields reconstructs blade occupancy conditioned on scene geometry, then converts predicted occupancy to $SE(3)$ poses via geometric scoring. The pipeline proceeds in three stages (Fig. 2): scene reconstruction and voxelization (Sec. 3.1), masked autoencoder training (Sec. 3.2), occupancy-to-pose conversion (Sec. 3.3), with an optional RGB distillation for inference efficiency (Sec. 3.4). The evaluation protocol is defined in Sec. 3.5.

We denote by $\mathcal{B}(P, b)$ the set of 3D points occupied by the blade body at pose $P \in SE(3)$ with extension $b \in \mathbb{R}_{\geq 0}$. *StowAffordance* dataset comprises N successful insertion cycles from production logs:

$$\mathcal{D} = \{O_i, \{(P_k^i, b_k^i)\}_{k=1}^K\}_{i=1}^N \quad (1)$$

where $O_i = \{I_i^{\text{rgb}}, I_i^{\text{d}}, \mathcal{P}_i, S_i\}$ is the RGB image, depth image, point cloud, and segmentation mask captured before blade contact. Three insertion strategies arise from production data (Table 1), each with one critical perceptual pose

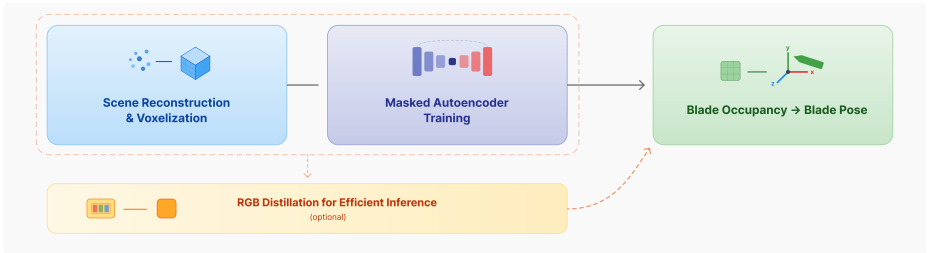


Fig. 2: VulcanVoxel pipeline. Depth observations are voxelized into multi-channel occupancy grids, then a masked autoencoder reconstructs blade occupancy from scene context. Predicted occupancy is converted to blade pose via geometric scoring. An optional RGB distillation path (bottom) replaces the explicit stages for efficient inference.

after which all subsequent motion relies on force feedback. A geometrically valid critical pose is necessary for the force-feedback phase to succeed.

Table 1: Insertion strategies with critical perceptual pose as the affordance prediction target. Motion primitives: APPROACH (move to bin opening), EXTENDBLADE (extend blade inside bin), ITEMPUSH (push the item inside to create initial clearance to seek the wall next to the item.), WALLSEEK (seek wall via force), FOLLOWWALL (translate along wall), LIPSEEK (seek bin lip, a stiff band at the bin bottom).

Strategy	Action Sequence	Critical Pose
Direct	APPROACH → EXTENDBLADE	EXTENDBLADE
Corner	APPROACH → EXTENDBLADE → WALLSEEK → (BIN)LIPSEEK	EXTENDBLADE
Wall	APPROACH → (ITEMPUSH) → WALLSEEK → FOLLOWWALL → EXTENDBLADE	WALLSEEK

We compare five models varying input representation, output representation, and training objective (Table 2). **RGB FM** predicts $SE(3)$ poses from RGB via flow matching. **PC FM** replaces RGB with a point cloud. **Voxel FM Pose** uses voxelized input with flow matching to predict poses. **Voxel FM Voxel** uses voxelized input and output with flow matching, sharing VulcanVoxel’s spatial output but not its reconstruction objective. **VulcanVoxel** reconstructs blade occupancy via masked autoencoder training. RGB FM vs. PC FM isolates input representation, Voxel FM Pose vs. Voxel FM Voxel isolates output representation, and Voxel FM Voxel vs. VulcanVoxel isolates the training objective.

3.1 Scene Representation

3D Bin Reconstruction. We reconstruct a scene mesh from a single RGB-D frame captured before blade contact. The depth image and known camera

intrinsic back-project into a point cloud \mathcal{P} , transformed to the bin frame via extrinsic calibration. MaskDINO [11] segments the RGB image, partitioning \mathcal{P} into per-object instance points $\{\mathcal{P}_i^{\text{obj}}\}$ and wall face points $\mathcal{P}_f^{\text{wall}}$ for $f \in \{\text{left, right, top, bottom, back}\}$.

Production bins exhibit fabric wall deformation of up to several centimeters. We correct for this by associating $\mathcal{P}_f^{\text{wall}}$ with each bin face using surface normals and signed distance from the nominal plane, then locally displacing mesh vertices to fit observed geometry, yielding a corrected wall mesh $\mathcal{M}^{\text{wall}}$.

Each object instance is reconstructed as a watertight mesh using TSDF fusion [4] applied to $\mathcal{P}_i^{\text{obj}}$ within the bin wall bounds. Unobserved surfaces (object bottoms, back faces) are completed by voxel carving against the enclosing wall mesh, yielding watertight surfaces without multi-view input. The full scene mesh is:

$$\mathcal{M}^{\text{all}} = \mathcal{M}^{\text{wall}} \cup \bigcup_i \mathcal{M}_i^{\text{obj}} \quad (2)$$

Multi-Channel Voxelization. We voxelize \mathcal{M}^{all} into a 32^3 occupancy grid over a $(30 \text{ cm})^3$ bounding box ($\sim 9.4 \text{ mm}$ per voxel), sufficient to resolve inter-object gaps ($\sim 15\text{--}30 \text{ mm}$) and blade cross-section geometry. Three channels encode distinct scene entities:

- O^{occupy} : combined wall and object occupancy.
- O^{object} : object occupancy only, enabling the model to distinguish wall-adjacent from object-adjacent free space.
- O^{blade} : blade occupancy at ground-truth pose (P_k, b_k) , defined as $O^{\text{blade}}(v) = \mathbf{1}[\mathcal{B}(P_k, b_k) \cap v \neq \emptyset]$.

Each channel O^x is accompanied by a binary mask indicator $M^x \in \{0, 1\}$, where $M^x = 1$ indicates the channel is masked and its values set to zero. This distinguishes genuine absence from masked occupancy during training. The full input tensor is:

$$\mathcal{V}^{\text{in}} = [O^{\text{occupy}}, O^{\text{object}}, O^{\text{blade}}, M^{\text{occupy}}, M^{\text{object}}, M^{\text{blade}}] \in \mathbb{R}^{6 \times 32^3} \quad (3)$$

3.2 VulcanVoxel: Masked Autoencoder for Blade Affordance

Masked Reconstruction as Affordance Learning. The inference query is spatial: given observed scene occupancy $(O^{\text{occupy}}, O^{\text{object}})$, reconstruct the geometrically consistent blade occupancy O^{blade} . Masked pretraining over all three channels forces the model to learn the geometry and semantics of bins, grounding blade placement in how walls, objects, and free space relate. Since each spatial location is evaluated independently with no global competition, multiple regions can be simultaneously activated, each satisfying local geometric compatibility. The result is a model that learns *where blades fit* rather than *where blades were inserted*, recovering multi-modal predictions from unimodal data.

Voxel FM Voxel shares the distributed spatial output but not the reconstruction objective, failing to create multi-modal predictions of the blade. Flow

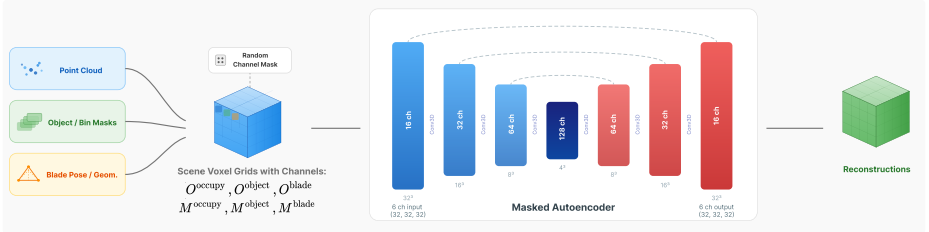


Fig. 3: VulcanVoxel architecture. Point cloud, object/bin masks, and blade geometry are used to construct a multi-channel 3D occupancy grid. During training, random channel masking is applied before the grid is passed through a 3D UNet autoencoder that reconstructs the masked channels.

matching denoises toward the training distribution, which is unimodal in occupancy space; operating in the spatial domain is necessary but not sufficient without a reconstruction objective that asks what is geometrically consistent rather than what was observed.

VulcanVoxel masks semantic channels rather than spatial patches [8]. Channel masking trains the model to infer one entity’s occupancy from another’s, directly matching the conditional structure of blade occupancy prediction from scene occupancy.

Training. We randomly mask one, two, or all three channels, sampling uniformly over all $2^3 - 1 = 7$ non-trivial masking patterns. Training on all patterns forces the model to learn inter-channel geometric relationships from multiple directions, preventing specialization to a single configuration. Loss is computed only over masked channels; at inference only the blade channel is masked, and $\hat{O}^{blade} \in [0, 1]^{32^3}$ is interpreted as a spatial probability distribution over geometrically consistent blade configurations.

Architecture. VulcanVoxel is a 3D U-Net with four stride-2 Conv3D encoder blocks ($6 \rightarrow 32 \rightarrow 64 \rightarrow 128 \rightarrow 256$ channels) compressing the 32^3 input to a $2^3 \times 256$ bottleneck, with a mirrored decoder and skip connections. Skip connections preserve fine-grained spatial detail necessary for localizing blade-sized free spaces.

Loss. Blade voxels are sparse ($< 3\%$ occupancy), so standard BCE loss produces degenerate predictions. We use Focal [12] and Dice [14] losses:

$$\mathcal{L} = \mathcal{L}_{\text{Focal}} + w_d \mathcal{L}_{\text{Dice}}, \quad w_d = 3.0 \quad (4)$$

$$\mathcal{L}_{\text{Focal}} = -\alpha_t (1 - p_t)^\gamma \log p_t, \quad \alpha = 0.85, \quad \gamma = 2.0 \quad (5)$$

$$\mathcal{L}_{\text{Dice}} = 1 - \frac{2|\hat{O}^{blade} \cap O^{blade}| + \epsilon}{|\hat{O}^{blade}| + |O^{blade}| + \epsilon}, \quad \epsilon = 1.0 \quad (6)$$

Focal loss down-weights well-classified empty voxels; Dice loss optimizes global region overlap, enforcing shape coherence. $w_d = 3.0$ was selected by grid search over $\{1, 2, 3, 5\}$ on a held-out validation set.

3.3 Inference: Occupancy to SE(3)

Pose extraction is a post-hoc projection from spatial affordances to pose parameters, deferred until after spatial reasoning is complete. We threshold \hat{O}^{blade} at $\tau = 0.5$ and identify connected components via 3D labeling. For each component we enumerate $N_\theta = 18$ candidate poses at 20° intervals about the insertion axis. Each candidate (\hat{P}, \hat{b}) is scored by volumetric overlap with the predicted field:

$$s(\hat{P}, \hat{b}) = \sum_v \hat{O}^{\text{blade}}(v) \cdot \mathbf{1}[\mathcal{B}(\hat{P}, \hat{b}) \cap v \neq \emptyset] \quad (7)$$

Blade extension \hat{b} is set to the connected component extent along the insertion axis, providing a geometry-driven estimate of insertion depth. Poses over empty predicted regions score poorly, enforcing the rigid-body constraint implicitly. Top- K poses are returned ($K = 1$ for accuracy, $K = 5$ for coverage evaluation).

3.4 RGB Distillation

Distillation serves two purposes: it provides generalization evidence that the teacher’s affordances are grounded in visually accessible geometric features rather than sensor-specific patterns, and it reduces inference from ~ 2.3 s to ~ 30 ms ($46\times$ speedup). We train a student $f_S : O^{\text{rgb}} \rightarrow \hat{O}_S^{\text{blade}}$ with:

$$\mathcal{L}_{\text{distill}} = \lambda \mathcal{L}(\hat{O}_S^{\text{blade}}, \hat{O}_T^{\text{blade}}) + (1 - \lambda) \mathcal{L}(\hat{O}_S^{\text{blade}}, O_{\text{GT}}^{\text{blade}}), \quad \lambda = 0.7 \quad (8)$$

$\lambda = 0.7$ prioritizes teacher supervision encoding multi-modal structure; the ground-truth term prevents mode over-smoothing. The student encoder is ViT-S/14 pretrained with DINO [3], producing 37×37 patch tokens of dimension 384. A 3D convolutional decoder lifts these to the 32^3 grid via positional encodings initialized from the known camera-to-bin transformation: each 2D patch token is associated with the column of voxels it projects onto in the bin frame, constraining 2D-to-3D lifting to physically meaningful patch-voxel pairs. This geometric constraint, absent in generic feature lifting [20, 21], substantially aids convergence.

Fig. 4 depicts sample blade occupancy visuals for voxel \rightarrow voxel masked model, and for RGB \rightarrow voxel distilled predictions.

3.5 Evaluation Protocol

Pose error against production labels is actively misleading: a prediction matching production pose may penetrate deformed bin walls, while one deviating substantially may be geometrically superior. SE(3) pose agreement is not a reliable proxy for geometric validity, which is a property of spatial occupancy. We evaluate all methods via cost over reconstructed bin meshes \mathcal{M}^{all} , sampling blade points $\mathbf{p} = \mathcal{S}(P, b)$ along three longitudinal profiles (top edge, centerline, bottom edge). The total cost $C_{\text{total}} = C_{\text{collision}} + C_{\text{reach}}$ combines:

$$C_{\text{collision}} = \sum_{e \in \mathcal{M}^{\text{all}}} w_e \text{ReLU}(m_e - \phi_e(\mathbf{p})) \quad (9)$$

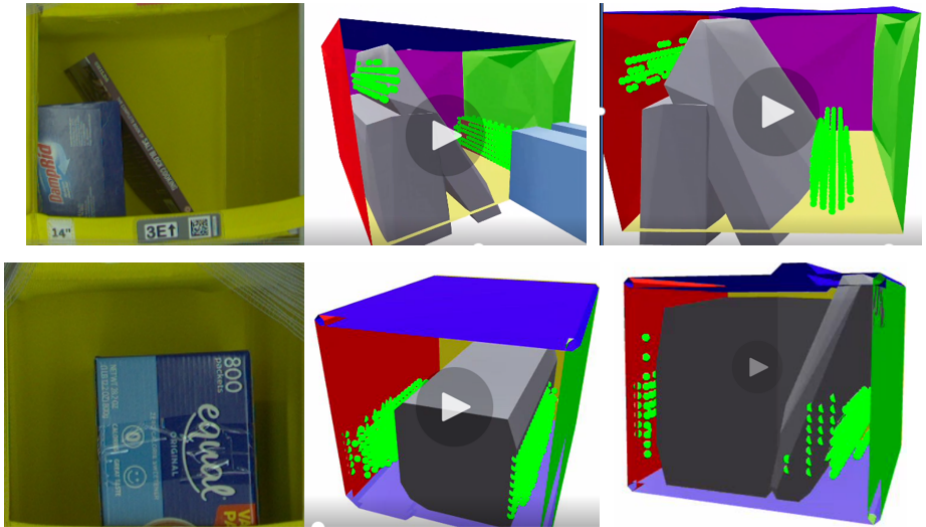


Fig. 4: VulcanVoxel Blade Prediction Visuals. Shown as green dots representing blade voxel occupancy within a rendering of the reconstructed bin-item 3D mesh. Bin walls are colored, items are in gray. **Top:** Bin image, Blade occupancy predictions for this image and another sample bin. **Bottom:** Vulcan Distill predictions for bin on the left and another sample bin.

where $\phi_e(\mathbf{p}) = \min_{\mathbf{q} \in \mathbf{p}} \text{SDF}_e(\mathbf{q})$, $m_e = 0.01 \text{ m}$, $w_e = 1.0$, with:

$$C_{\text{reach}} = \text{ReLU}(\bar{x}_{\text{obj}} - x_{\text{tip}}) \quad (10)$$

where \bar{x}_{obj} is the mean object centroid depth and x_{tip} is the blade tip depth in the bin frame. For Wall Insert the left/right wall margin increases to 0.05 m and the reach cost is omitted, as the critical pose is a wall contact point. These terms directly reflect production failure modes: back-wall penetration, lateral collision, and insufficient reach.

Production executions achieve $C_{\text{total}} = 0.63$ on our test set. We use $C_{\text{total}} < 1.0$ as the validity threshold for coverage evaluation, set at one standard deviation above the production mean. This accommodates geometrically valid predictions that differ in execution style from production while remaining within a safe operating envelope. $C_{\text{total}} < 1.0$ is a necessary condition for geometric validity of the perceptual decision, not a sufficient condition for task success, as force-feedback dynamics after initial insertion are not captured in our dataset. Cost differences between VulcanVoxel and most baselines (0.81 vs. 2.08–3.57 on Direct Insert) far exceed plausible reconstruction error magnitudes, confirming that performance differences reflect genuine geometric reasoning. The one baseline achieving lower cost (0.60) produces sharply unimodal predictions, collapsing to a single strategy rather than recovering the full set of valid placements.

Table 2: Methods. VV Distill is evaluated separately in Sec. 4.5.

Method	I/O	Obj.	ms↓
RGB FM	RGB→Pose	FM	72
PC FM	PC→Pose	FM	399
VoxFMPose	Voxel→Pose	FM	412
VoxFMVox	Vox.→Pose	FM	418
VulcanVoxel	Vox.→Vox	MAE	2300
VV Distill	RGB→Vox.	Distill.	30

4 Experiments

We address four questions. **Q1** Does VulcanVoxel produce operationally valid poses versus baselines? **Q2** Does spatial inference recover multi-modal predictions, and which properties drive this? **Q3** Do affordances generalize across time and clutter? **Q4** Does VulcanVoxel generalize to configurations that challenged the production system and led to stow failures?

4.1 Experimental Setup

StowAffordance dataset comprises $\sim 20,000$ successful insertion cycles from May–June 2025 (training) and 1,000-cycle test sets from July and August 2025. Temporal separation ensures evaluation on unseen configurations. The primary test set contains 508 Direct, 288 Corner, and 204 Wall Insert cycles. Each episode provides RGB-D observations before blade contact, executed SE(3) poses and blade extensions, and outcome labels.

Table 2 summarizes all methods. All flow matching models use identical U-Net architectures with FiLM conditioning and 100 denoising steps at test time; 100 independent noise-initialized samples are drawn per scene for coverage evaluation. All models train with Adam ($\text{lr} = 1 \times 10^{-4}$, batch 32) on a single V100 for 100 epochs. RGB images are cropped to a $0.3 \text{ m} \times 0.3 \text{ m}$ field of view and zero-padded to 518×518 , matching the $(30 \text{ cm})^3$ voxel bounding box. Augmentation is limited to random horizontal flip; vertical flip and color jitter disrupt the geometric patch-voxel correspondence exploited by the distilled student.

We report two metrics. *Single-prediction cost* C_{avg} is the C_{total} of the top-ranked prediction. *Top- K coverage*:

$$\text{Cov}_K = \frac{1}{N} \sum_{i=1}^N \mathbf{1} \left[\min_{k \leq K} C_{\text{total}}(\hat{P}_k^i) < 1.0 \right] \quad (11)$$

measures the fraction of scenes where at least one of K predictions falls within the production cost envelope ($C_{\text{total}} < 1.0$, one standard deviation above the production mean of 0.63). Cov_K captures the operational value of spatial inference: diverse predictions covering independent insertion regions increase the probability that at least one candidate is geometrically valid when a planning system selects among options. We report Cov_5 as the primary coverage metric.

Table 3: Operational cost and top-5 coverage, July 2025 (1,000 cycles). C_{avg} : mean single-prediction cost. Viol: hard violations (any mesh penetration exceeding safety margin $m_e=0.01\text{m}$). Cov_5 : fraction of scenes with at least one valid pose among top 5. Production (Prod) generates one prediction per scene; Cov_5 not applicable. †Wall Insert omits reach cost.

	Direct (508)			Corner (288)			Wall† (204)		All	
	$C\downarrow$	Viol \downarrow	$\text{Cov}_5\uparrow$	$C\downarrow$	Viol \downarrow	$\text{Cov}_5\uparrow$	$C\downarrow$	Viol \downarrow	$C\downarrow$	Viol \downarrow
Production	0.63	0	—	1.39	0	—	0.77	0	0.88	0
RGB FM	3.57	207	0.21	6.11	223	0.09	2.68	110	4.27	540
PC FM	2.08	58	0.44	2.72	53	0.31	1.15	14	2.06	125
Voxel FM Pose	0.60	3	0.71	1.18	0	0.68	0.25	0	0.72	3
Voxel FM Voxel	3.13	100	0.19	4.45	75	0.14	1.23	20	2.99	195
VulcanVoxel	0.81	5	0.89	1.08	4	0.86	0.42	2	0.79	11

Table 4: Multi-modality metrics, July 2025. σ : mean pairwise tip distance (cm). N_m : mean cluster count. Cov: valid coverage fraction. VulcanVoxel is the only method achieving high diversity ($\sigma > 7\text{cm}$), multiple modes ($N_m > 2$), and high valid coverage simultaneously.

	Direct			Corner			Wall		
	$\sigma\uparrow$	$N_m\uparrow$	Cov \uparrow	$\sigma\uparrow$	$N_m\uparrow$	Cov \uparrow	$\sigma\uparrow$	$N_m\uparrow$	Cov \uparrow
RGB FM	1.2	1.0	0.08	0.9	1.0	0.04	1.4	1.0	0.11
PC FM	3.1	1.2	0.19	2.4	1.1	0.12	3.8	1.3	0.24
Voxel FM Pose	0.8	1.0	0.67	0.6	1.0	0.63	0.7	1.0	0.71
Voxel FM Voxel	2.3	1.1	0.07	1.8	1.0	0.05	2.6	1.2	0.09
VulcanVoxel	8.4	2.7	0.71	7.1	2.4	0.68	9.2	3.1	0.74

4.2 Main Results (Q1)

Table 3 reports evaluation on 1,000 July 2025 test cycles. VulcanVoxel achieves the highest Cov_5 across all strategies while matching production on C_{avg} . On Corner Insert it surpasses production (1.08 vs. 1.39), avoiding unnecessarily conservative wall-approaching behavior.

Single-prediction accuracy and coverage diversity trade off fundamentally. Voxel FM Pose achieves the lowest C_{avg} (0.60/1.18/0.25) but all five predictions cluster identically ($N_m = 1.0$, Table 4); when its top prediction fails, all five fail. VulcanVoxel’s marginally higher C_{avg} (0.81/1.08/0.42) comes with predictions covering independent insertion regions, achieving $\text{Cov}_5 = 0.89/0.86/0.83$ versus 0.71/0.68/0.74.

The baseline progression traces the domain argument directly. RGB FM produces 540 violations from back-wall penetrations: appearance alone cannot reason about insertion depth in 3D space. PC FM reduces violations to 125 and raises Cov_5 to 0.44: richer geometric input helps but is insufficient without spa-

tial inference. Voxel FM Voxel, despite sharing VulcanVoxel’s distributed spatial output, achieves only $\text{Cov}_5 = 0.19$ with 195 violations: flow matching denoises toward the unimodal training distribution even in occupancy space, confirming that operating in the spatial domain is necessary but not sufficient without the reconstruction objective.

4.3 Multi-Modal Prediction Analysis (Q2)

For each method we generate 100 candidate poses per scene and compute spatial spread σ_{tip} (mean pairwise blade tip distance, cm), mode count N_m (DBSCAN, $\epsilon = 3$ cm, min size 5), and valid coverage Cov_{100} . Table 4 reports results.

RGB FM and Voxel FM Pose are both unimodal ($N_m = 1.0$); their Cov_{100} contrast (0.08 vs. 0.67) reflects accuracy not diversity. PC FM shows marginally more spread (3.1 cm): geometric input helps but is insufficient without spatial domain reasoning. Voxel FM Voxel achieves higher spread (2.3 cm) but near-zero valid coverage (0.07): spread without the reconstruction objective yields geometrically incoherent alternatives. VulcanVoxel alone achieves high spread ($\sigma = 8.4$ cm), multiple modes ($N_m = 2.7$), and high valid coverage ($\text{Cov}_{100} = 0.71$) simultaneously.

The Voxel FM Voxel vs. VulcanVoxel contrast is the most diagnostic: identical distributed spatial output, different objective. The gap ($N_m: 1.1 \rightarrow 2.7$; $\text{Cov}_{100}: 0.07 \rightarrow 0.71$) directly evidences the reconstruction objective as the critical factor beyond operating in the spatial domain. This result has a clean interpretation in terms of the domain argument. Voxel FM Voxel operates in the spatial domain but optimizes a generative objective: it learns to denoise toward the observed occupancy distribution, which is unimodal because each training episode records one executed placement. VulcanVoxel optimizes a reconstruction objective: it learns what occupancy is geometrically consistent with the scene, a question that admits multiple valid answers independent of what was executed. The domain is the same; the question asked is different.

4.4 Generalization (Q3, Q4)

Temporal (August 2025). Fig. 5(left) shows method rankings fully preserved two months after training. VulcanVoxel improves slightly on Direct Insert (0.81 \rightarrow 0.78), indicating no overfitting to July conditions.

High clutter (GCU > 50%). Fig. 5(right) evaluates 222 high-clutter cycles. All methods degrade, including production (Corner: 2.29 vs. 1.39), consistent with smaller free-space gaps. VulcanVoxel maintains the highest Cov_5 across all strategies. The Cov_5 advantage over Voxel FM Pose grows under clutter (0.71 vs. 0.54), confirming that multi-modal spatial coverage is most valuable when free-space volumes are most constrained.

Challenging configurations (Q4). We evaluate on 180 production failure cycles from August 2025 (61 Direct, 80 Corner, 39 Wall) in Fig. 6(left). Failures have multiple causes beyond affordance errors (calibration drift, force-feedback failures, mechanical issues), so these represent a challenging generalization test

	Direct (500)		Corner (304)		Wall† (196)	
	$C_{avg}\downarrow$	$Cov_5\uparrow$	$C_{avg}\downarrow$	$Cov_5\uparrow$	$C_{avg}\downarrow$	$Cov_5\uparrow$
Production	0.67	—	1.46	—	0.40	—
RGB FM	3.71	0.19	5.35	0.08	2.98	0.23
PC FM	2.31	0.41	2.86	0.28	1.27	0.52
Voxel FM Pose	0.66	0.73	1.18	0.69	0.64	0.74
Voxel FM Voxel	3.21	0.17	4.44	0.13	1.27	0.41
VulcanVoxel	0.78	0.91	1.29	0.84	0.37	0.88

	Direct (78)		Corner (57)		Wall† (87)	
	$C_{avg}\downarrow$	$Cov_5\uparrow$	$C_{avg}\downarrow$	$Cov_5\uparrow$	$C_{avg}\downarrow$	$Cov_5\uparrow$
Production	1.01	—	2.29	—	0.22	—
RGB FM	3.54	0.18	5.95	0.07	3.22	0.16
PC FM	3.62	0.22	3.59	0.19	1.41	0.44
Voxel FM Voxel	3.43	0.21	6.02	0.11	1.25	0.38
VulcanVoxel	1.95	0.71	2.24	0.68	0.47	0.79

Fig. 5: Left: Generalization to August 2025 (1,000 cycles). Method rankings preserved across the two-month temporal gap. **Right:** High clutter (GCU > 50%, July 2025). VulcanVoxel degrades less in coverage than competing methods; the Cov_5 advantage over Voxel FM Pose grows under clutter. (†Wall Insert omits reach cost.)

	Direct (61)		Corner (80)		Wall† (39)	
	$C_{avg}\downarrow$	$Cov_5\uparrow$	$C_{avg}\downarrow$	$Cov_5\uparrow$	$C_{avg}\downarrow$	$Cov_5\uparrow$
RGB FM	4.02	0.14	3.80	0.11	3.53	0.12
PC FM	1.44	0.38	2.81	0.22	0.64	0.51
Voxel FM Voxel	2.70	0.16	4.41	0.10	1.12	0.31
VulcanVoxel	0.55	0.87	0.92	0.83	0.43	0.81

	Direct			Corner		
	$C_{avg}\downarrow$	$Cov_5\uparrow$	$N_m\uparrow$	$C_{avg}\downarrow$	$Cov_5\uparrow$	$N_m\uparrow$
RGB FM	3.57	0.21	1.0	6.11	0.09	1.0
VV Distill	1.84	0.69	1.9	2.31	0.61	1.7
VulcanVoxel	0.81	0.89	2.7	1.08	0.86	2.4

Fig. 6: Left: Challenging configurations (production failures, August 2025). VulcanVoxel maintains coverage consistent with the successful test set while all baselines degrade substantially. Results represent a generalization test on difficult bin configurations, not a failure correction benchmark. **Right:** Distillation quality, July 2025. VV Distill substantially outperforms RGB FM at comparable speed, preserving partial multi-modality and $\sim 65\%$ of teacher prediction quality.

rather than a failure correction benchmark. The geometric validity of VulcanVoxel’s predictions on these cycles ($Cov_5 > 0.80$) suggests that many production failures are attributable to execution-phase errors rather than perceptual errors, consistent with the force-feedback and calibration causes identified in the failure logs.

VulcanVoxel achieves $Cov_5 > 0.80$ across all strategies, consistent with the successful test set, while all baselines degrade to $Cov_5 < 0.40$. VulcanVoxel’s lower C_{avg} on failure cases (0.55/0.92) than on successful ones (0.81/1.08) reflects the cost metric’s scope: calibration and force-feedback failures appear geometrically valid under a metric limited to the perceptual decision.

4.5 Distillation

Fig. 6(right) evaluates distillation quality and provides generalization evidence for the teacher. The student achieves teacher-student IoU of 0.41 versus teacher-GT IoU of 0.63, recovering $\sim 65\%$ of teacher prediction quality from RGB alone. A depth-free student matching teacher predictions on held-out bins confirms that the teacher’s affordances are grounded in visually accessible geometric features rather than sensor-specific patterns, precisely the evidence that spatial inference has learned geometric structure rather than execution-specific

correlations. The student recovers $N_m = 1.9$ modes versus the teacher’s 2.7; the reduction is consistent with monocular depth ambiguity limiting discrimination of depth-separated insertion regions. $\text{Cov}_5 = 0.69$ on Direct Insert is $3.3\times$ higher than RGB FM at comparable speed, in 30 ms ($46\times$ speedup over the full pipeline).

5 Conclusion

Blade affordances are spatial objects and should be inferred in their native domain. Learning them from unimodal production data requires keeping inference in 3D space rather than projecting into $\text{SE}(3)$ pose coordinates, where geometric feasibility is no longer directly computable. Spatial reconstruction over 3D occupancy fields recovers multi-modal predictions from inherently unimodal observations by learning where blades fit as a local geometric condition rather than where blades were inserted as a global pose distribution.

Key findings. VulcanVoxel achieves $\sigma = 8.4$ cm spread and $N_m = 2.7$ modes per scene versus single-mode predictions from all baselines, with $\text{Cov}_5 = 0.89$ versus 0.71 for the best pose-based method. Single-prediction accuracy and coverage are complementary: Voxel FM Pose leads on C_{avg} while VulcanVoxel leads decisively on Cov_5 . The Voxel FM Voxel contrast is the most diagnostic result: identical spatial output representation, different objective, Cov_{100} from 0.07 to 0.71. Operating in the spatial domain is necessary but not sufficient; the reconstruction objective is what activates the domain advantage. A 30 ms RGB student recovering 65% of teacher quality confirms the teacher has learned geometrically grounded rather than execution-specific affordances.

Broader significance. Blade insertion is a canonical instance of free-space affordance learning for rigid tool use, complementary to the well-studied surface contact affordance problem. The core argument extends beyond stowing: tool affordances are spatial objects, and inferring them in $\text{SE}(3)$ pose space discards the geometric structure most relevant to feasibility reasoning. This applies to any manipulation domain where geometric compatibility is the core constraint, and suggests that spatial inference is the natural default wherever production data is abundant even if unimodal.

Limitations. The 32^3 voxel resolution (~ 9.4 mm) may miss fine geometric features, and single-view reconstruction introduces depth ambiguity for occluded surfaces. The cost function does not capture force-feedback dynamics after initial insertion, and the distilled student cannot resolve depth ambiguity for bin configurations outside the training distribution.

StowAffordance. We released a dataset at https://www.armbench.com/blade_insertion.html, containing 10,000+ blade insertion episodes with RGB-D observations, $\text{SE}(3)$ trajectories, and production outcome labels.

Acknowledgements

Tianyu Li, as a PhD student from UPenn, performed this work as a summer intern funded by the Vulcan Stow team in Amazon Robotics.

References

1. Bahl, S., Mendonca, R., Chen, L., Jain, U., Pathak, D.: Affordances from human videos as a versatile representation for robotics. In: Proceedings of the IEEE/CVF Conference on Computer Vision and Pattern Recognition (CVPR) (2023)
2. Cao, A.Q., de Charette, R.: MonoScene: Monocular 3d semantic scene completion. In: Proceedings of the IEEE/CVF Conference on Computer Vision and Pattern Recognition (CVPR) (2022)
3. Caron, M., Touvron, H., Misra, I., J'egou, H., Mairal, J., Bojanowski, P., Joulin, A.: Emerging properties in self-supervised vision transformers. In: Proceedings of the IEEE/CVF International Conference on Computer Vision (ICCV) (2021)
4. Curless, B., Levoy, M.: A volumetric method for building complex models from range images. In: Proceedings of SIGGRAPH (1996)
5. Fang, K., Chen, Y., et al.: SAGA: Open-world mobile manipulation via structured affordance grounding. <https://arxiv.org/abs/2512.12842> (2025)
6. Fishman, A., Murali, A., Eppner, C., Peele, B., Boots, B., Fox, D.: CabiNet: Scaling neural collision detection for object rearrangement with procedural scene generation. In: IEEE International Conference on Robotics and Automation (ICRA) (2023)
7. Gkanatsios, N., Xu, J., Bronars, M., Mousavian, A., Ke, T.W., Fragkiadaki, K.: 3d flowmatch actor: Unified 3d policy for single-and dual-arm manipulation. arXiv preprint arXiv:2508.11002 (2025)
8. He, K., Chen, X., Xie, S., Li, Y., Doll'ar, P., Girshick, R.: Masked autoencoders are scalable vision learners. In: Proceedings of the IEEE/CVF Conference on Computer Vision and Pattern Recognition (CVPR) (2022)
9. Hudson, N., Hooks, J., et al.: Stow: Robotic packing of items into fabric pods. arXiv preprint arXiv:2505.04572 (2025)
10. Ke, T.W., Gkanatsios, N., Fragkiadaki, K.: 3D diffuser actor: Policy diffusion with 3d scene representations. In: Conference on Robot Learning (CoRL) (2024)
11. Li, F., Zhang, H., Liu, H., Guo, J., Ni, L.M., Zhang, L.: Mask DINO: Towards a unified transformer-based framework for object detection and segmentation. In: Proceedings of the IEEE/CVF Conference on Computer Vision and Pattern Recognition (CVPR) (2023)
12. Lin, T.Y., Goyal, P., Girshick, R., He, K., Doll'ar, P.: Focal loss for dense object detection. In: Proceedings of the IEEE/CVF International Conference on Computer Vision (ICCV) (2017)
13. Mescheder, L., Oechsle, M., Niemeyer, M., Nowozin, S., Geiger, A.: Occupancy networks: Learning 3d reconstruction in function space. In: Proceedings of the IEEE/CVF Conference on Computer Vision and Pattern Recognition (CVPR) (2019)
14. Milletari, F., Navab, N., Ahmadi, S.A.: V-Net: Fully convolutional neural networks for volumetric medical image segmentation. In: International Conference on 3D Vision (3DV) (2016)

15. Mo, K., Guibas, L., Mukadam, M., Gupta, A., Tulsiani, S.: Where2act: From pixels to actions for articulated 3d objects. In: Proceedings of the IEEE/CVF International Conference on Computer Vision (ICCV) (2021)
16. Qian, S., Mo, K., Blukis, V., Fouhey, D.F., Fox, D., Goyal, A.: 3d-mvp: 3d multi-view pretraining for manipulation. In: Proceedings of the IEEE/CVF conference on computer vision and pattern recognition. pp. 22530–22539 (2025)
17. Simeonov, A., Du, Y., Tagliasacchi, A., Tenenbaum, J.B., Rodriguez, A., Agrawal, P., Sitzmann, V.: Neural descriptor fields: SE(3)-equivariant object representations for manipulation. In: IEEE International Conference on Robotics and Automation (ICRA) (2022)
18. Tang, Y., Huang, W., et al.: UAD: Unsupervised affordance distillation for generalization in robotic manipulation. <https://arxiv.org/abs/2506.09284> (2025)
19. Turpin, D., Wang, L., Bhatt, R., Garg, A.: GIFT: Generalizable interaction-aware functional tool affordances without labels. In: Robotics: Science and Systems (RSS) (2023)
20. Wang, Y., Li, Z., Zheng, M., Driggs-Campbell, K., Li, F.F., Savarese, S., Li, Y.: D3Fields: Dynamic 3d descriptor fields for zero-shot generalizable rearrangement. In: Conference on Robot Learning (CoRL) (2024)
21. Wilcox, A., Ghanem, M., et al.: Adapt3R: Adaptive 3d scene representation for domain transfer in imitation learning. <https://arxiv.org/abs/2503.04877> (2025)
22. Wu, R., Chen, K., Geng, C., Dong, H.: Learning environment-aware affordance for 3d articulated object manipulation under occlusions. In: Advances in Neural Information Processing Systems (NeurIPS) (2023)
23. Wu, R., Zhao, Y., Gupta, A., Huang, D.A., Fang, H.S., Li, J., Guibas, L., Dong, H.: VAT-Mart: Learning visual action trajectory proposals for manipulating 3d articulated objects. In: International Conference on Learning Representations (ICLR) (2022)
24. Zeng, A., Florence, P., Tompson, J., Welker, S., Chien, J., Attarian, M., Armstrong, T., Krasin, I., Duong, D., Sindhwani, V., Lee, J.: Transporter networks: Rearranging the visual world for robotic manipulation. In: Conference on Robot Learning (CoRL) (2020)